PAPER • OPEN ACCESS

Investigation of ELM-related Larmor ion flux into toroidal gaps of divertor target plates

Investigation of ELM-related Larmor ion flux into toroidal gaps of divertor target plates

K. Krieger[1,*], **M. Balden**[1], **M. Barac**[2], **I. Bogdanović Radović**[2], **D. Brida**[1], **M. Faitsch**[1], **J.P. Gunn**[3], **S. Markelj**[4], **M. Kelemen**[4], **A. Manhard**[1], **P. de Marne**[1], **R.A. Pitts**[5], **V. Rohde**[1], **the ASDEX Upgrade Team**[a] **and the EUROfusion MST1 Team**[b]

[1] Max-Planck-Institut für Plasmaphysik, Boltzmannstr. 2, 85748 Garching, Germany
[2] Rudjer Bošković Institute, Bijenička cesta 54, 10000 Zagreb, Croatia
[3] CEA, IRFM, 13108 Saint-Paul-Lez-Durance, France
[4] Jožef Stefan Institute, Jamova cesta 39, Ljubljana, 1000, Slovenia
[5] ITER Organization, Route de Vinon-sur-Verdon, CS 90 046, 13067 Saint-Paul-Lez-Durance Cedex, France

E-mail: karl.krieger@ipp.mpg.de

CrossMark

Abstract

A detailed assessment of the thermo-mechanical limits of the International Tokamak Experimental Reactor (ITER) divertor with respect to potential excessive local transient heat loads due to edge localised modes (ELMs) has revealed a particular power loading scenario arising from the fact that ELM ions expelled from the upstream pedestal region will arrive at the divertor target plates without substantial thermalisation. As a consequence of their Larmor gyration around magnetic field lines, they are able to penetrate toroidal gaps between individual monoblocks of the target plate structure and can deliver rather intense heat loads to monoblock side faces near the gap entrance. To verify that this ELM-induced loading, predicted by both ion orbit simulations and particle in cell simulations, really does occur, two dedicated experiments have been performed on the ASDEX Upgrade tokamak. In both experiments a model toroidal gap structure of similar dimensions to those of the ITER divertor target monoblocks was exposed to a series of identical H-mode discharges with strong type-I ELMs. The effects arising from the gyro motion of hot ELM ions were identified by inverting, in the second experiment, the directions of both toroidal field and plasma current, thus reversing the ion gyration direction. The local distribution of incident ion flux on the gap side faces was quantified by pre- and post-exposure analysis of platinum marker layers to determine quantitatively the erosion rate of the platinum marker. The results fully confirm the ion orbit code predictions with respect to the penetration depth of incident ions with gyro orbits of similar or larger radius than the gap width. Moreover, the results confirm that ELM ions do indeed arrive at the divertor with their typical pedestal energies and also allow conclusions to be drawn regarding the corresponding intra-ELM ion particle and power flux, which is not easy to quantify using Langmuir probes.

1. Introduction

In tokamaks designed for sustained thermo-nuclear plasma discharges such as the International Tokamak Experimental Reactor (ITER), the engineering concept of the high heat flux divertor target area is based on actively cooled poloidally-running (i.e. vertical with respect to gravity) tungsten monoblock stacks with a central water cooling tube [1]. In the case of ITER, these monoblocks are separated by toroidally-running gaps of 0.4 mm width (see figure 2 in [2]). Similarly, the individual monoblock stacks (plasma-facing units—PFUs) are separated by a poloidally-running gap of the same width (see figures 1 and 2 in [3]). The castellated structure of the plasma-facing components is chosen principally for the reduction of thermo-mechanical stress forces.

A disadvantage of the castellations is that the monoblock side faces near the gap entrances are partially exposed to the full thermal plasma parallel heat flux, which, because of the oblique angle of the magnetic field at the target plate surface, can exceed the design limit of the surface heat load by an order of magnitude, potentially driving local overheating and ultimately melting. For the poloidally oriented gaps between PFUs this can be avoided by modifying the flat rectangular monoblock design to one with a slight toroidal inclination of the plasma exposed surface so that any poloidal leading edges are in the geometric shadow cast by the magnetic field lines and are thus mostly protected from the parallel plasma flux [1].

For the final design before the procurement phase [4], the shaping of the ITER divertor monoblocks was optimised by predictive simulations of the local power flux footprint based on the optical projection of the magnetic field lines to the target surface, but also including the effect of the ion gyro motion [5–7]. The latter is necessary because ions expelled by edge localised modes (ELMs) from the hot plasma pedestal region into the scrape-off layer (SOL) are predicted, according to the free streaming model (FSM) of ELM propagation [8, 9], to not fully thermalise on their way to the divertor, thus arriving at the target plates with a significant fraction of their pedestal thermal energy. This has in fact been directly linked to the observed intra-ELM W sputtering flux on the JET [10–12] and DIII-D [13, 14] tokamaks. For ITER, typical intra-ELM ion temperatures of up to 5 keV [5] are expected in baseline burning plasma discharges at $Q_{DT} = 10$. For the nominal toroidal magnetic field of 5.3 T in ITER [4], this corresponds to a Larmor gyration radius of O(1 mm) for D or T ions, which is comparable to and even exceeds the typical gap widths between the monoblocks in the high heat flux areas of the vertical targets. The combination of ion gyro motion and pitch angle of the magnetic field is predicted to lead to significant heat loads due to the ion Larmor flux component at the near gap entrance

side faces of the toroidally oriented monoblocks. Moreover, because of the gyro motion of the hot ions their respective power flux component at the ITER inner vertical target (IVT) will be directed oppositely to the direction of the geometric field line projection onto the target surface [5–7] (see figure 5 in [5] for a schematic view). As a consequence it is not possible to protect exposed edges of toroidal monoblock gaps at the IVT by any additional shaping of the monoblocks, which introduces additional constraints on plasma operation in order to limit the expected surface damage by local overheating of edges [7].

The predictions from the ion orbit modelling code, which only considers the ion dynamics due to the magnetic field, were benchmarked against particle in cell (PIC) simulations, which also include the local sheath and pre-sheath electric field and its influence on ion orbits in the underlying physics model [15]. It turned out that over the expected range of plasma parameters, there are no significant discrepancies between the two modelling approaches [15], suggesting that the effect of the near-surface electric field is indeed sufficiently small to justify the simplifying assumptions for the ion orbit modelling.

In light of the potential consequences of these predictions, experiments were planned and carried out in several current fusion devices in an attempt to validate the respective codes. One experimental approach consists of measuring the local temperature distribution near toroidally oriented gaps of dedicated plasma-facing components with castellated surfaces using high spatial resolution infra-red (IR) cameras. Such experiments were performed in the KSTAR tokamak [16], although with inconclusive outcome, and subsequently in the COMPASS tokamak [17, 18]. The experiments at COMPASS provided the first conclusive evidence for the heating of the toroidal gap edges by ion Larmor flux. This was demonstrated by alternating the gyro direction of the ion orbits in subsequent plasma discharges with opposite directions of magnetic field and plasma current [17, 18]. The evidence gained from these observations is, however, still indirect, because the heat flux contributions of ions and electrons cannot be distinguished by the IR measurements. Moreover, the observed sample was located not at a divertor target plate but on specially designed tiles on the COMPASS central column and exposed in L-mode discharges in limiter configuration with the magnetic field adjusted to provide an ion gyro radius of similar magnitude to the gap width. Further experimental confirmation was therefore desirable for divertor conditions with type-I ELM transients in which the ELM-related hot pedestal ions provide the main contribution to the power and particle load to the geometrically shadowed monoblock side faces near the gap entrance.

To overcome the limitations of studies based on IR observations, the experiments presented in this paper were designed to

provide direct evidence for the flux of ELM-related ions into toroidally oriented gaps of castellations at the divertor target plate. This was realised by measuring the erosion of marker layers deposited on the highly polished side faces of dismountable castellated samples. The lateral distribution of the marker erosion not only allows quantitative conclusions on the ion flux and ion energy to be drawn but also provides direct evidence for the predicted impact pattern of the ion Larmor fraction of the power flux under the exposure conditions expected at the ITER IVT. As in the COMPASS experiments, the ion orbit effects were confirmed by alternating the ion gyro direction in two subsequent exposures with reversed magnetic field and current directions.

Section 2 of the paper describes the experimental setup and the plasma parameters of the chosen discharge scenarios. In section 3 the results of the marker erosion measurements are presented. Their interpretation and comparison with respective code simulations are discussed in section 4.

2. Experimental setup

2.1. Sample design

The default probe head of the ASDEX Upgrade outer divertor manipulator [19] allows two adjacent full-size sample tiles of identical geometry to the standard target tiles to be simultaneously exposed. The probe head can be retracted from its exposure position to an airlock chamber where the probe head assembly, or alternatively individual tiles, can be exchanged in between experiment days without breaking the torus vacuum. To ensure that samples are only exposed to the plasma discharges of a particular experiment, the remaining discharges of the respective day are generally restricted to limiter and upper divertor configurations.

Since the Larmor ion flux penetration into toroidally oriented gap structures is expected to be mainly a function of the local plasma parameters and of the width of the gap, potential dependencies from these parameters were studied by installing in total four gap samples at two different poloidal positions and with two different gap widths, 0.5 mm (original ITER design value, meanwhile reduced to 0.4 mm) and 1 mm, respectively. One tile on the manipulator probe head was equipped with the 0.5 mm gap samples and the second tile with the 1 mm samples at identical poloidal positions. The samples, with a toroidal extent of 30 mm, were designed as two detachable elements made of molybdenum (Mo) with a steel spacer in between creating the desired gap width. This allowed the samples to be disassembled for pre-exposure layer preparation and characterisation and then for post-exposure surface analysis of the interior gap side faces. Figure 1 shows a CAD view of an assembled tile (*a*) and the technical design of the sample (*b*).

Molybdenum was chosen as base material firstly because of its compatibility with the expected high power flux close to the plasma strike point during exposure and secondly because its atomic mass is below that of platinum (Pt) used for the erosion marker. This facilitates the surface analysis by ion beam Rutherford back-scattering spectroscopy (RBS). The
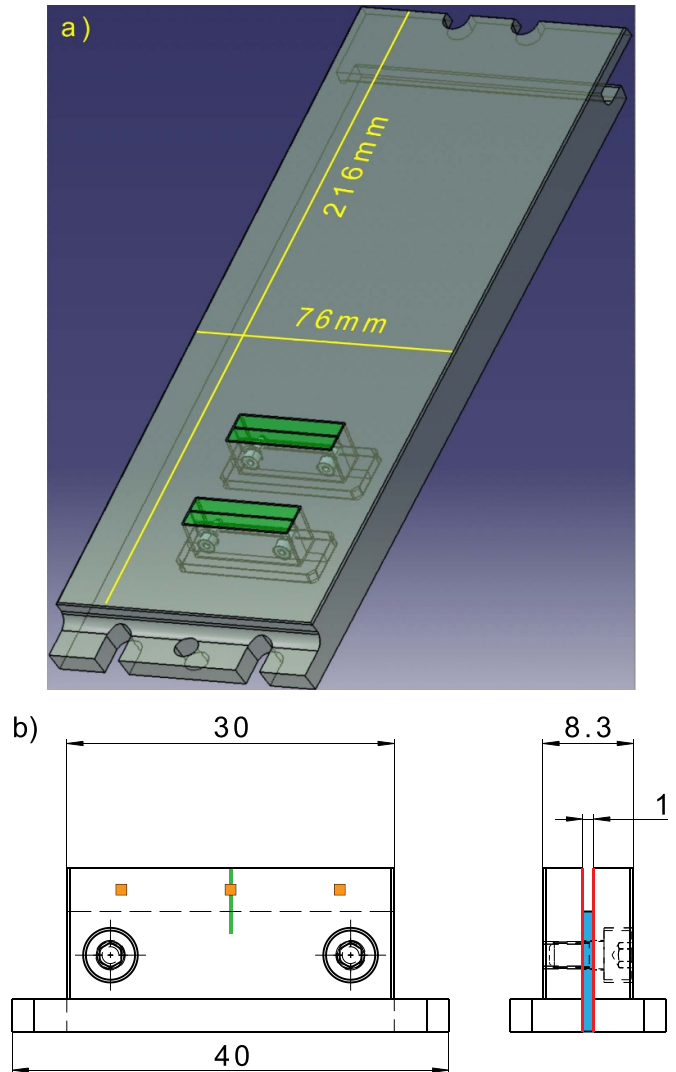
Figure 1. (*a*) CAD view of target tile with samples installed. (*b*) Sample technical design in the toroidal and poloidal planes with Pt marker coating indicated by red lines and the steel spacer creating the gap marked in blue. The orange markers indicate the points where the Pt marker layers were analysed pre-exposure by RBS and the green line shows the location of the post-exposure marker analysis.

inner side faces of the gap samples were first polished to a mirror finish. Then the Pt marker layers were established on these surfaces by physical vapour deposition (PVD) at a nominal thickness of 20 nm for the first experiment and 50 nm for the second experiment. The increased thickness for the second experiment was motivated by the observed full erosion of the Pt marker layer near the gap entrance in the first experiment.

2.2. Discharge scenario

In order to verify the Larmor ion flux impact pattern predicted for ITER with the plasma conditions available in deuterium discharges in the smaller ASDEX Upgrade device, a discharge scenario was chosen with suitably high pedestal temperature to produce ELM ions which, in the lower magnetic field of
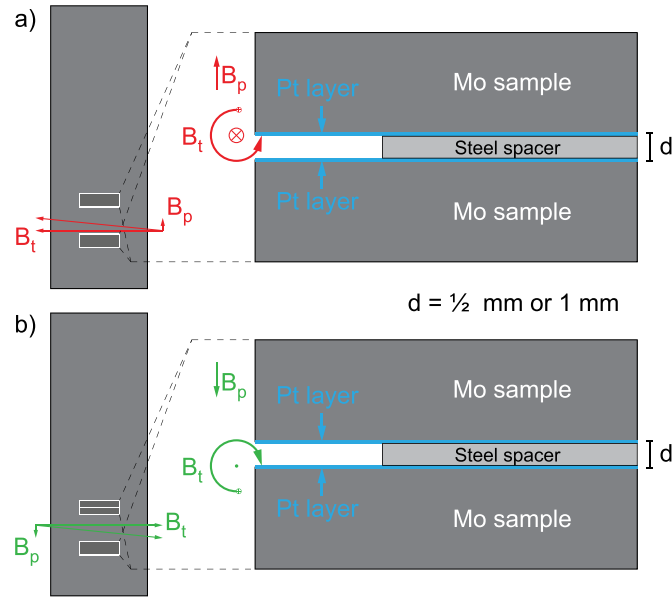
Figure 2. Schematic frontal view of the ASDEX Upgrade outer divertor manipulator target plate seen from the plasma side (left) and of the toroidal sample cross-section (right). The directions of magnetic field and of ion gyration are shown for reversed (*a*) and default (*b*) I_p and B_t configurations, respectively.

Table 1. Key parameters of the two ASDEX Upgrade experiments with default and reversed directions of plasma current and toroidal magnetic field, respectively. ECRH stands for electron cyclotron resonance heating, NBI for neutral beam injection, f_{ELM} denotes the ELM frequency and ΔE_{ELM} the average ELM-induced plasma stored energy loss.

| Experiment type/AUG discharges	Plasma current I_p (MA)	Toroidal field B_t (T)	Line averaged density $\bar{n}_e$ (10^{19} m^{-2})	NBI power (MW)	ECRH power (MW)	Sample exposure time (s)	f_{ELM} (Hz)	ΔE_{ELM} (kJ)
Reversed I_p and B_t #37336–#37343	−0.8	+2.5	$3.0 \rightarrow 4.4$	5.0	5.0	20.2	134	12
Default I_p and B_t #38852–#38857	+0.8	−2.5	$4.2 \rightarrow 4.8$	5.0	4.5	25.6	133	20

ASDEX Upgrade, have gyro orbit radii comparable to those in ITER (for D-ions in ITER [6]: $T_i = 5$ keV, $B_t = 6$ T, $r_L = 1.7$ mm, in AUG: $T_i = 1$ keV, $B_t = 2.6$ T, $r_L = 1.75$ mm, using characteristic values of T_i at pedestal top and of B_t at outer divertor target). Since both devices have an identical field line topology at the divertor target plates and given that sample exposure in ASDEX Upgrade is only possible at the outer divertor target, the first experiment with the same ion orbit orientation at the toroidal gap as that at the ITER IVT had to be performed in ASDEX Upgrade with reversed directions of toroidal magnetic field and plasma current (see figure 2(*a*)). The second experiment was performed with discharges in the default ASDEX Upgrade magnetic field and current configuration to verify the corresponding reversal of ion impact pattern at the toroidal gap (see figure 2(*b*)). Apart from the directions of toroidal field and plasma current, the nominal discharge parameters (table 1) and plasma geometry of both scenarios were identical. It should be noted that a perfect match of plasma parameters and H-mode properties in both regimes was not expected because of transport differences arising from the respective relative directions of plasma flows and drifts,

as discussed in [20]. It was assumed, however, that these differences would not affect the principal observations, as subsequently confirmed by the experimental results.

Figure 3 shows time traces of several key plasma parameters for the reversed I_p and B_t configuration (*a*) and for the default I_p and B_t configuration (*b*). To avoid oscillations from the feedback between active density control and ELM frequency, both scenarios were designed with a pre-programmed feed-forward gas feed trajectory. As a downside, the resulting plasma density was not perfectly stationary but increased over the duration of the discharge, leading to minor variations of plasma radiation losses and plasma stored energy.

For discharge startup and to establish the diverted plasma shape, the outer strike point position (OSP) was programmed above the location of the gap samples and moved to a position approximately 1 cm below the lower gap sample during the plasma flat-top phase before it was finally moved again above the two samples for plasma ramp down (see figure 3, row ④). For the reversed I_p and B_t experiment, eight discharges were executed, resulting in a total exposure time of the gap samples of ≈20.2 s. In the subsequent experiment with default
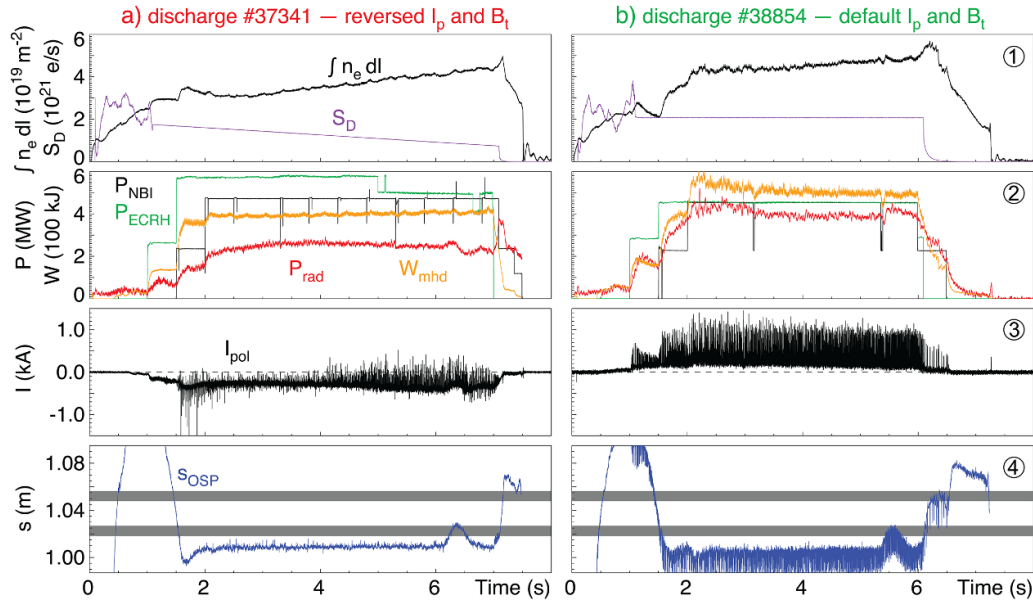
Figure 3. Time traces of plasma parameters, (*a*) for reversed I_p and B_t configuration, (*b*) for default I_p and B_t configuration. Quantities shown are in row ①: line averaged electron density $\int n_e dl$ and total deuterium gas fuelling rate S_D, row ②: NBI heating power P_{NBI}, ECRH power P_{ECRH}, total radiated power P_{rad} and plasma stored energy W_{MHD}, row ③: poloidal current into outer target plate I_{pol} used as an ELM signature and row ④: position of the OSP on the outer divertor target plate s_{OSP}. The shaded areas in plot ④ represent the positions of the two gap samples.
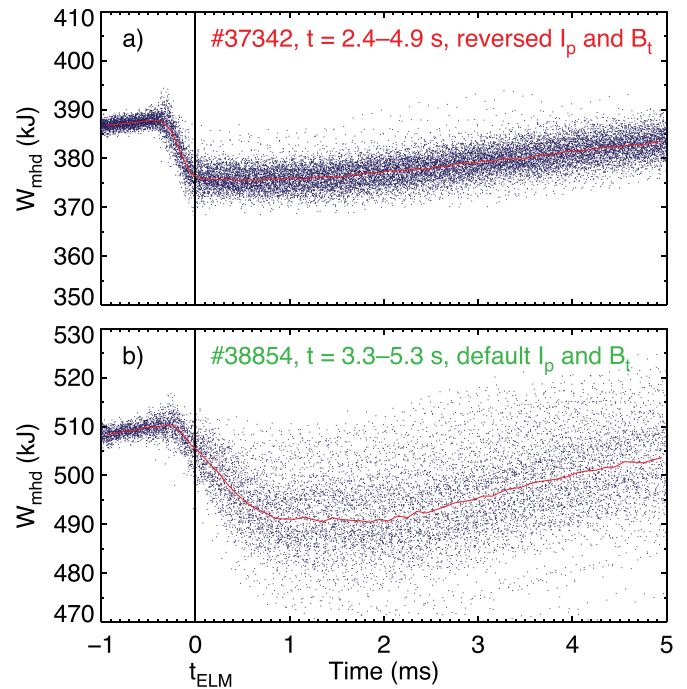
I_p and B_t configuration, discharges were longer, with a resulting total gap sample exposure time of ≈ 25.6 s obtained in only six discharges.

The average loss of stored plasma energy by the ELMs, ΔE_{ELM}, was determined for both experiments by coherent averaging over the ELMs during the discharge flat top phase, as shown in figure 4. Due to the higher energy confinement in the default I_p and B_t configuration, the plasma stored energy is about 30% larger in these discharges despite their higher total radiation losses (figure 3, row ③). While the ELM frequency in both the default and reversed I_p and B_t configurations is approximately the same (see table 1), ΔE_{ELM} is again about 30% larger in the default I_p and B_t configuration, although spread out over a longer ELM relaxation time.

2.3. Plasma pedestal parameters

For the H-mode scenario with type-I ELMs used in this study, it has been shown that the ELM properties at the target plate are closely linked to the upstream pedestal plasma parameters (see e.g. [21]). On ASDEX Upgrade, pedestal electron density and electron/ion temperature profile data are acquired by a number of diagnostics such as Thompson scattering, Li-beam spectroscopy and charge-exchange recombination spectroscopy using the NBI injectors as neutral D sources [22]. Of particular relevance for the data analysis and interpretation of the gap erosion data are the ion temperature T_i and the electron pressure p_e at the pedestal top, which is, in ASDEX Upgrade, usually defined to be at normalised radius $\rho_{pol} = 0.95$.

The ion temperature in the pedestal region is an important factor in determining the energy of the ELM ions arriving at the target plates. Respective profiles are shown in figure 5

Figure 4. Plasma stored energy coherent average over time intervals $[-1\,\text{ms}, +5\,\text{ms}]$ relative to onset of ELMs during the discharge flat top phase of example discharges in reversed I_p and B_t configuration ((*a*), $\langle \Delta E_{ELM} \rangle = 12.3\,\text{kJ}$) and default I_p and B_t configuration ((*b*), $\langle \Delta E_{ELM} \rangle = 19.9\,\text{kJ}$).

for the two experiment scenarios, with estimated values at the pedestal top of $T_i \approx 1.2$ keV (figure 5(*a*)) for reversed and $T_i \approx 1.0$ keV (figure 5(*b*)) for the default I_p and B_t configuration. The ion temperatures were in both experiments derived
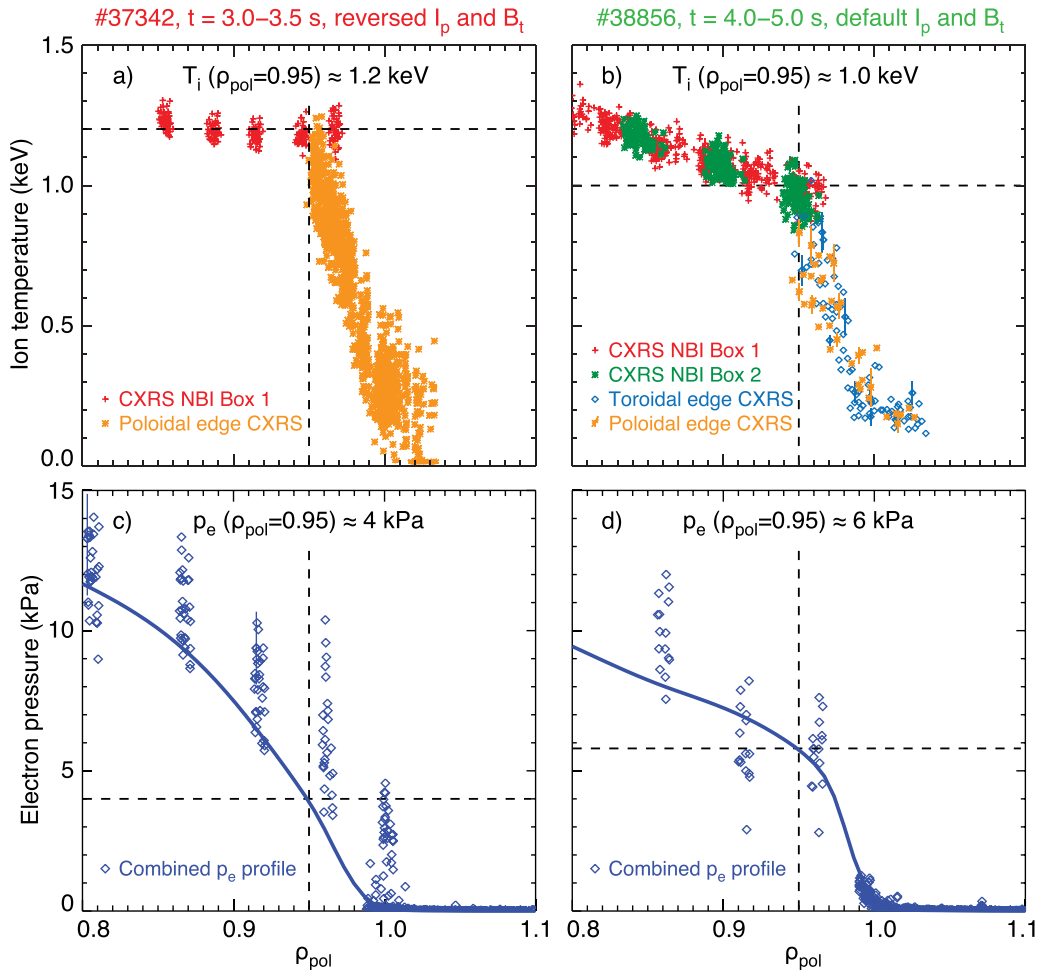
Figure 5. Pedestal profiles of T_i (upper row, (*a*) and (*b*)) and p_e (lower row, (*c*) and (*d*)). The plots on the left ((*a*) and (*c*)) show the profiles for reversed I_p and B_t configuration, those at the right ((*b*) and (*d*)) for the default configuration. The solid curve in plots (*c*) and (*d*) denotes the result of the high level integrated data analysis (IDA) diagnostic, while the dots represent pressure values computed directly from the temperature and density raw data.

from CX recombination spectral lines of B^{5+} ions assuming $T_i \simeq T_{B^{5+}}$, which is justified by the energy equilibration time between impurities and main ions being much shorter than the local transport time scale [23].

The value of p_e can be used to estimate the intra-ELM plasma density and electron temperature at the target plate (see section 2.4), which cannot be measured directly by the divertor Langmuir probes. Profiles of p_e in the pedestal region are determined by an integrated data analysis approach, which derives the pressure profile as an optimal fit to the available temperature and density data [24]. Corresponding results are shown in figure 5 for the two experiment scenarios, with p_e at the pedestal top ≈ 4 kPa (figure 5(*c*)) for reversed and ≈ 6 kPa, (figure 5(*d*)) for the default I_p and B_t configuration. It should be noted that these profiles represent the average over the entire analysed time interval without conditional averaging over the ELMs. This might underestimate the pressure right before the onset of the ELMs, particularly in the reversed I_p and B_t case, as indicated by the scatter in the pressure data computed directly from the temperature and density raw signals.

Using p_e, an estimate of the average ELM parallel energy density in the SOL can be obtained using the scaling law derived in [21, 25], which can be deployed to cross-check local IR-thermography measurements of the power flux at the target plates. With $\epsilon_\parallel \cong 6\pi \times p_e \times R_{geo} \times q_{edge}$ (equation (9) in [21]), $R_{geo} = 1.62$ m and $q_{edge} = \sqrt{(1+\kappa^2)/2} \times a_{geo}/R_{geo} \times B_{tor}/B_{pol} \approx 2.3$ for reversed—and ≈ 2.2 for default I_p and B_t, one obtains $\epsilon_\parallel \approx 0.28$ MJ m^{-2} (reversed I_p, B_t) and $\epsilon_\parallel \approx 0.40$ MJ m^{-2} (default I_p, B_t). Values for a_{geo}, κ, B_{tor} and B_{pol} were taken from the equilibrium reconstruction for the discharges and time points referenced in table 2 with the magnetic field components taken at the major radius of the low-field side separatrix contour at the height of the magnetic axis.

2.4. Local plasma parameters at outer target plate

Local plasma parameters and magnetic field geometry at the outer target plate determine the characteristic properties and the direction of the incident ion and electron flux, both for

Table 2. Local magnetic field geometry at the centre of the gap entrance slits. B_x (B_y) denote the magnetic field components along the tile surface in the horizontal (vertical) directions, B_z the magnetic field component perpendicular to the tile surface. Apart from the sign, the magnetic field components are identical for both configurations to within the first three digits. The values are derived from the magnetic equilibrium reconstructions for discharges 37341@5.5 s (reversed I_p, B_t config., sign(B_x) = −1) and 38854@4.0 s (default I_p, B_t config., sign(B_x) = +1). Also listed are the resulting angles between the magnetic field and target plate surface, φ, and the vertical pitch angle of the magnetic field in the plane of the outer target plate surface, θ. s is the position of the respective gap on the poloidal divertor contour with the lower edge of the outer target tile at $s = 0.987$ m and the upper edge at $s = 1.203$ m (see figure 1(*a*)).

s (m)	B_x (T)	B_y (T)	B_z (T)	φ	θ
1.054	∓2.58	±0.08	±0.09	2.1°	1.85°
1.023	∓2.60	±0.08	±0.10	2.3°	1.75°

the guiding centre motion and the gyro-orbit orientation. The magnetic field geometry can be obtained from the ASDEX Upgrade magnetic equilibrium reconstruction [26]. As shown in figure 6 the plasma configuration in the flat-top phase of both experiments was very well reproducible with near perfect match of the flux surfaces. This also holds for the local pitch angle of the magnetic field and its angle to the surface of the outer target plate (figure 2), with values for the two sample positions during plasma flat-top phase given in table 2 as input for the modelling of the incident ion and electron flux distribution described in section 4.

The local electron flux, density and temperature are derived from Langmuir probe measurements [27]. Due to the limited battery voltage of the probe diagnostic power supply, the divertor triple probes in ASDEX Upgrade cannot acquire the full ion saturation current during ELMs. Therefore, both j_{sat} and T_e are generally only available for the inter-ELM phases of H-mode discharges. Using the measured poloidal current into the outer target plate (figure 3, row ③) as an indicator for the ELM time intervals, the respective data points in the Langmuir probe data can be filtered out. The resulting inter-ELM profiles of Γ_i, derived from j_{sat}, and of T_e are shown in figure 7 for both experiments. Unfortunately, the Langmuir probe at the poloidal position of the lower gap samples was defective during the reversed I_p and B_t experiment, while during the default I_p and B_t discharges it did not provide data of sufficient quality for the evaluation of T_e. For the reversed I_p and B_t scenario, additional T_e data were available from adjacent swept single probes, although acquired with much lower time resolution (2.4 ms vs. 45 μs for triple probe data).

With the measured inter-ELM values of ion flux and electron temperature at the gap locations, the expected inter-ELM erosion of the Pt marker layers can be computed for comparison with the measured total erosion fluence in section 4.

For estimates of the intra-ELM particle flux and temperature, the power flux derived from IR measurements can be used under the very good assumption that the SOL is essentially collisionless during ELMs, i.e. in the sheath limited regime (see section 4). The particle flux can then be extrapolated from the
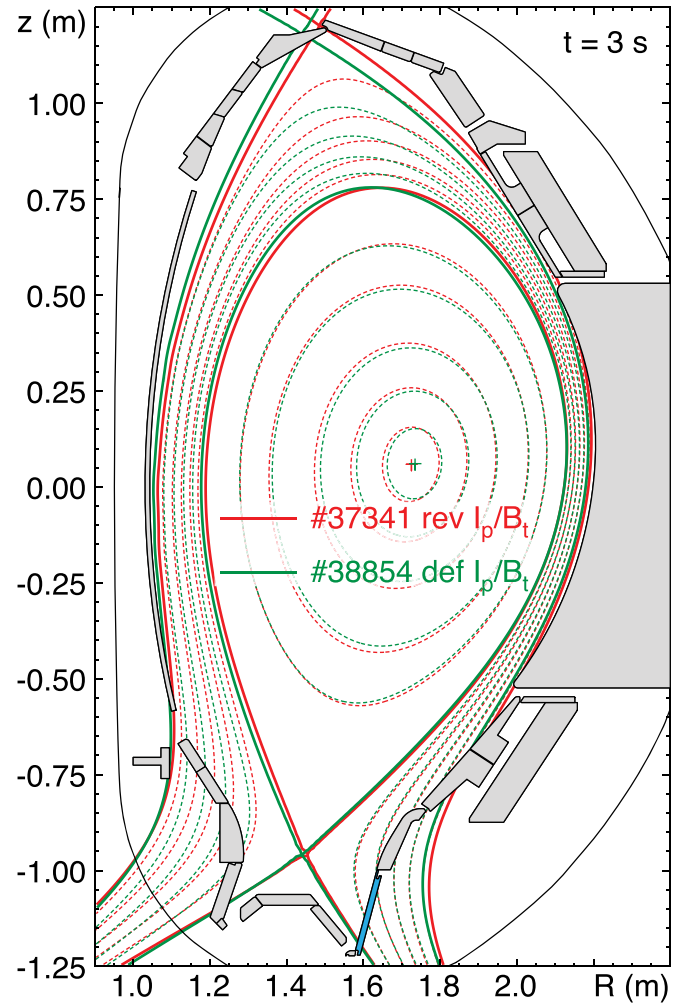
Figure 6. Magnetic equilibrium reconstructions during the flat-top phase for reversed (red) and default (green) I_p and B_t configurations. The outer divertor target plate is highlighted in blue.

local power flux and upstream pedestal density and temperatures, although with some unavoidable ambiguity with respect to the local values of T_e vs. T_i at the target. Figure 8 shows overlays of intra-ELM power flux profiles during discharge flat-top phases acquired in the time intervals 0.5–1 ms after the onset of each ELM. The large scatter of the data points is caused on the one hand by the radial variations of the individual ELM filament positions, and on the other, by the limited data acquisition rate of the IR camera (≈2 kHz) with exposure times of O(10 μs), so that for each individual ELM there are only a few time slices available. Hence the temporal evolution of the local intra-ELM power flux at the positions of the gap samples was derived by conditional averaging over all ELMs in the same discharge time windows as processed to generate figure 8. The results are shown in figure 9 for the time interval [−1, +4] ms relative to the ELM onset. Evidently, the ELMs in the reversed I_p, B_t configuration are a factor ≈2 shorter than in the default configuration, while the ELM peak power is correspondingly higher.

Integrating over the average ELM time trace one obtains at the position of the lower gap a parallel ELM energy
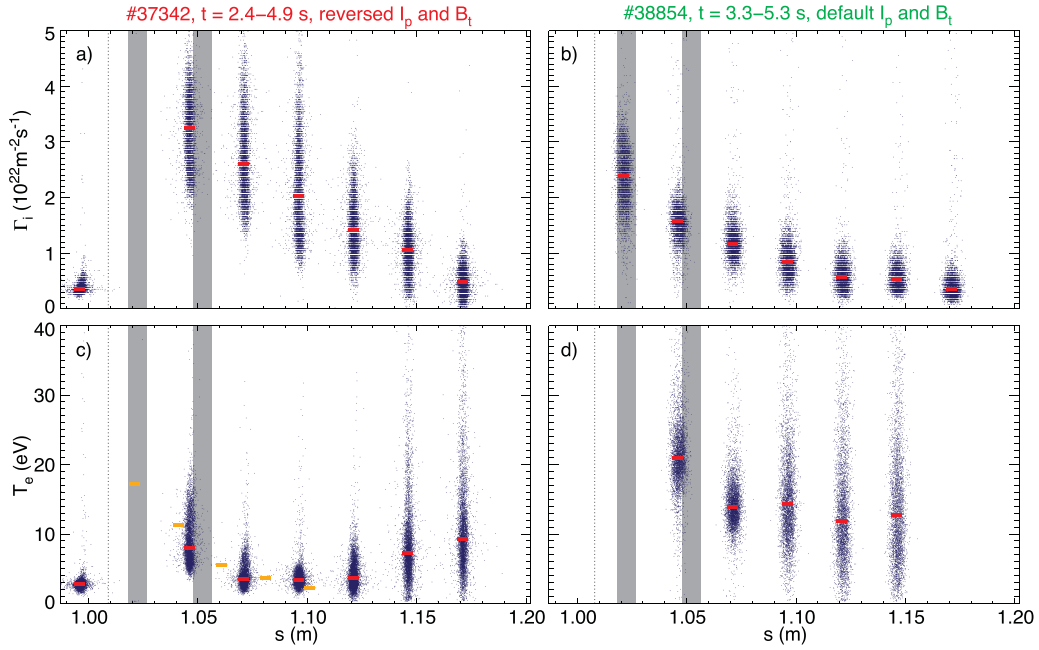
Figure 7. Coherent overlay of inter-ELM Langmuir probe data from time windows 1.0–0.3 ms before the ELM onset. Plots (*a*) and (*b*) show ion flux, Γ_i, plots (*c*) and (*d*) electron temperature, T_e. The plots on the left (*a*) and (*c*) are for reversed I_p and B_t configuration (#37342, $t =$ 2.4–4.9 s), those at the right ((*b*) and (*d*)) for default I_p and B_t configuration (#38854, $t =$ 3.3–5.3 s). The red bars represent the median values of the individual probe data. Additional orange markers in (*c*) represent median T_e values evaluated from swept single probes acquired in the same time interval. The width of the markers corresponds to the poloidal width of the probe tips.

density of 1.2 MJ m^{-2} for the reversed I_p, B_t configuration and 0.8 MJ m^{-2} in default configuration whereas at the position of the upper gap this is already considerably smaller at 0.35 MJ m^{-2} and 0.31 MJ m^{-2} for the respective cases. Given the uncertainty of a factor 3 in the ELM parallel energy scaling in [21], these values inferred from the IR target measurements are entirely consistent with the scaling.

The intra-ELM ion flux can be obtained from the relation $q = (\gamma T_e + E_{rec})\Gamma_i$ with the sheath transmission factor $\gamma \approx 4.85(1 - R_E) + 2.15$ where R_E is the energy reflection coefficient of D ions (≈ 0.2 at $E = 1$ keV) and $E_{rec} = 13.6 +$ 5.5/2 eV the recombination energy per ion [28]. Of more interest for comparison with the measured marker erosion is the ion fluence per ELM, Φ_{ELM}. In the reversed I_p, B_t configuration the ELM energy density on the target surface, $q_\perp$ is 47.5 kJ m^{-2} (lower gap) and 12.8 kJ m^{-2} (upper gap) resulting in intra-ELM hot ion fluences of $\Phi_{ELM} = 7.1 \times 10^{19}$ m^{-2} and 1.9×10^{19} m^{-2}, respectively. In the default I_p, B_t configuration, the corresponding ELM energy densities are 32 kJ m^{-2} (lower gap) and 11.4 kJ m^{-2} (upper gap), yielding hot ion fluences of $\Phi_{ELM} = 4.8 \times 10^{19}$ m^{-2} and 1.7×10^{19} m^{-2}, respectively.

3. Marker erosion measurements

The lateral distribution of the Pt marker layer erosion was determined by pre- and post-exposure ion beam analysis (IBA) and scanning electron microscopy (SEM). The former allows the area density of a given element to be quantified by detecting either the energy spectra of back-scattered probe ions in

the MeV energy range (Rutherford back-scattering spectroscopy, RBS) or by measuring the characteristic x-ray emission from inner shell transitions of the target atoms excited by high energy protons, i.e. proton induced x-ray emission spectroscopy (PIXE). X-ray analysis can also be performed in a scanning electron microscope by exciting the target atoms with the microscope's electron beam (electron dispersive x-ray spectroscopy, EDX), although one has to take into account that for thicker deposited layers, electron attenuation may introduce significant errors.

3.1. Pre-exposure characterisation

Prior to sample exposure, the Pt marker layer thickness on the polished gap sides was characterised in the IPP tandem accelerator laboratory using RBS with He$^+$ ions. The variation of layer thickness across the samples was determined by measuring at three points on each sample, at the centre of the sample and ± 10 mm on either side, along a line 2 mm from the gap edge (see figure 1(*b*)). The measurements represent the average Pt area density across the 1 mm^2 beam cross-section.

For the samples exposed in the first experiment with a nominal Pt marker thickness of 20 nm, RBS analysis was performed with a 1 MeV ^{4}He beam. The mean value of the Pt area density was determined to 126.5×10^{15} at cm^{-2}. Assuming the solid state density of Pt, this corresponds to an actual layer thickness of 19 nm. The thickness varied slightly between samples with a standard deviation of 5.6% due to slight lateral variations of the deposition rate, which cannot be entirely eliminated by the rotating sample tray in the PVD device used to the deposit the layer. For the second set of samples with
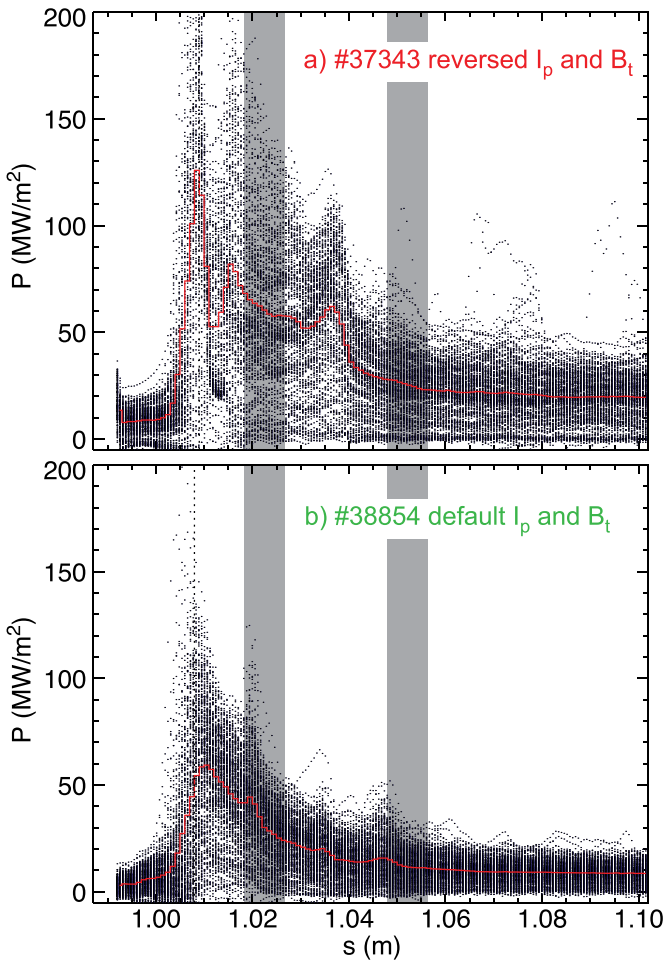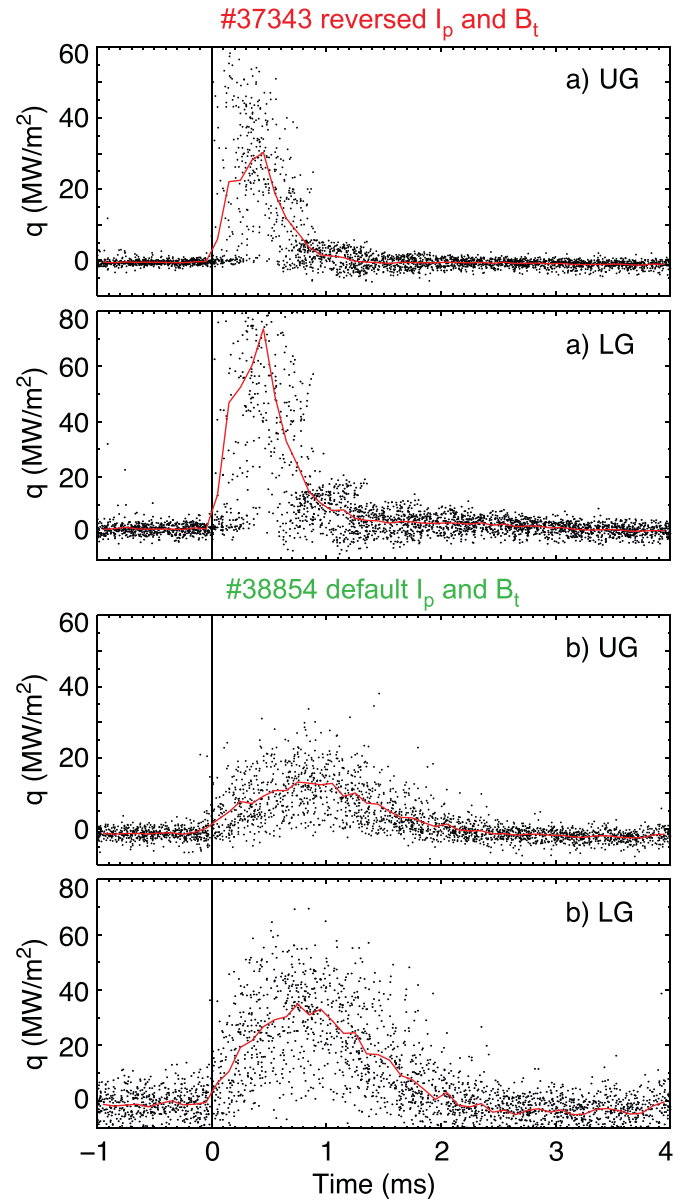
Figure 8. Coherent overlay of intra-ELM power flux data from thermography for (*a*) reversed I_p and B_t configuration (discharge 37343, $t = 2.5$–4.5 s, 0.3–0.6 ms from onset of ELM) and (*b*) default I_p and B_t configuration (discharge 38854, $t = 3.3$–5.3 s, 0.5–1.0 ms from onset of ELM). The red lines represent the average over the accumulated ELM data points, vertical black lines denote position of OSP and shaded bars denote position of gap samples. The local maximum between the two sample positions in the reversed I_p and B_t configuration is an artefact of the IR measurements due to increased surface emissivity caused by deposited low-Z impurities. The local minimum just outside the OSP position is also an artefact caused by saturation of the detector and corresponding constant apparent temperature manifesting itself in the thermography analysis as vanishing power flux.

Figure 9. Coherent overlay of intra-ELM power flux data from thermography relative to onset of ELMs for (*a*) reversed I_p and B_t configuration (discharge 37343, $t = 2.5$–4.5 s) and (*b*) default I_p and B_t configuration (discharge 38854, $t = 3.3$–5.3 s). The red lines represent the average over the accumulated ELM data points. Data from lower gap position are labelled by LG, those from the upper gap position by UG.

a nominal marker thickness of 50 nm, RBS analysis was performed with a 2.5 MeV ^{3}He beam. For these samples the mean Pt area density was 339.8×10^{15} at cm^{-2}, corresponding to 51 nm with a standard deviation between samples of 6.4%. For both sets of samples the uniformity across an individual sample was even better, with a standard deviation in the range of 0.5%–3.5%.

In addition to the RBS analysis, the homogeneity of the Pt layers on length scales below the dimension of the ion beam cross-section was confirmed down to O($10\,\mu$m) by EDX analysis at several locations across the samples.

The uniformity of the marker layers greatly simplified subsequent post-exposure analysis because respective Pt thickness measurements could be normalised and compared directly to the average pre-exposure thickness values.

3.2. Post-exposure visual inspection

After exposure, the condition of the marker layer was first documented by light microscopy using an Olympus LEXT 4000 Confocal Laser Scanning Microscope (CLSM). Figure 10 shows the resulting images assembled from a series of scans across the inner gap sample surfaces. On all samples clear indications of deposited material extending into the gaps up to the area covered by the steel spacers during exposure are
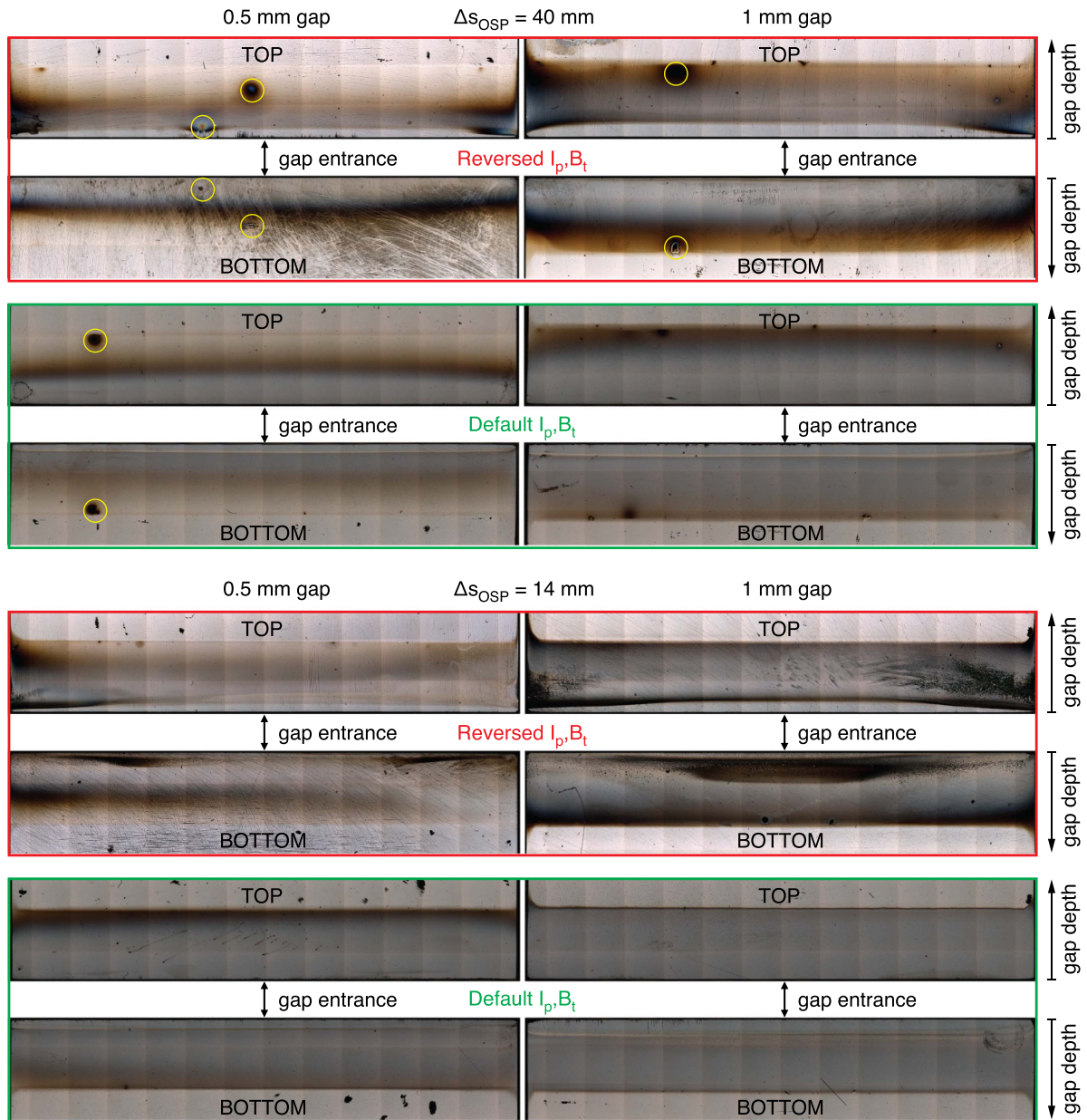
Figure 10. CLSM images of gap side faces after exposure. Samples exposed in the reversed I_p, B_t and in the default I_p, B_t discharges are marked by red and green frames, respectively. Yellow circles indicate visible traces of arcs burning between opposite side faces.

found. Subsequent ion beam nuclear reaction analysis, NRA, (section 3.4) revealed the presence of carbon (C) in the deposits. Other residual low-Z impurity species, such as oxygen (O) or boron (B), the latter from glow discharge boronisation used for wall conditioning in ASDEX Upgrade, were below the detection threshold because of their much smaller ^{3}He nuclear reaction cross-sections compared to that of the ^{12}C isotope. Already from the visual impression, a clearly visible narrow zone of apparent re-erosion (or at least lower net-deposition) can be identified at the gap entrance, correlated to the direction of incident Larmor ions, i.e. at the top side face of the gap samples exposed in discharges with reversed I_p and B_t and at the bottom side face of the gap samples exposed in discharges with default I_p and B_t. For quantitative confirmation of this visual evidence, the lateral profile of remaining

post-exposure marker layer thickness was measured from the gap entrance downwards, extending also to the area of the marker shielded by the steel spacer, for normalisation to the pre-exposure marker thickness. All measurements discussed here were taken at the centre of the gap area marked by the green line in figure 1(b). For comparison, a few profiles were also measured along lines 5 mm from the end of the gap samples on each side. Apart from minor variations attributed to 3D shadowing effects, these showed no significant differences to the profiles measured at the centre.

On the gap side faces a number of arc traces can also be seen, with the more prominent cases found at identical positions on opposite gap sides. These were apparently stationary, pointing to ignition during wall conditioning glow discharges since arcs ignited during plasma discharges are

typically observed to move over O(0.1–1 mm) distances perpendicular to the magnetic field [29], which was aligned in these experiments approximately horizontally along the samples. The affected parts of the surface are, however, small and therefore had no noticeable influence on the SEM and ion beam measurements.

3.3. Post-exposure SEM analysis

As a first step of quantitative post-exposure characterisation, the samples were analysed in the Helios (FEI) and Auriga (ZEISS) SEM microscopes at IPP Garching. The relative abundance of both Pt in the marker layer and W deposited in the gap during plasma exposure were determined by EDX. X-ray spectra were acquired at 30 keV acceleration voltage with electron beam scans across rectangular areas of $250 \times 210 \ \mu m^2$ from the gap entrance down into the gap up to a depth of 5 mm where the Pt layer was shielded against plasma impact by the sample's steel spacer. The latter data point was initially assumed to still represent the pre-exposure marker thickness, although subsequent analysis revealed that the marker layer had been slightly damaged by the mechanical pressure of the spacer against the surface. It turned out, however, no Pt erosion was detectable beyond a gap depth of $d = 3$ mm on any of the samples so that the data from that position were used for normalisation. For each data point the peak integrals of the Pt L_α-line at $E = 9.44$ keV and of the W L_α-line at $E = 8.40$ keV in the acquired x-ray spectrum were computed and then normalised to the Pt intensity at $d = 3$ mm. The resulting profiles of both normalised Pt layer thickness and W deposition are shown in figure 11 with EDX data plotted with red markers whose width corresponds to the scan range of $210 \ \mu m$. Since there is no sufficiently accurate model for the penetration of the 30 keV electrons into the material and their corresponding energy loss, constant x-ray line excitation coefficients over the layer depth range cannot be assumed. The EDX measurements were therefore complemented by additional micro-beam analysis described in the next section.

3.4. Post-exposure micro-beam analysis

Following the SEM measurements, the samples were subsequently sent to RBI Zagreb and then to JSI Ljubljana for further analysis using their micro-IBA capabilities. At RBI the samples were analysed by PIXE, using the same Pt and W L_α transitions as for the EDX analysis conducted at IPP. For the measurements a 2 MeV proton beam was focused on a surface spot of $10 \times 10 \ \mu m^2$. X-ray emission spectra were collected by a Si(Li) detector placed at an angle of $135°$ to the incident beam. To attenuate the strong Mo L line emission from the bulk material, a $50 \ \mu m$ Kapton foil was placed in front of the Si(Li) detector. X-ray maps were collected by scanning the beam across the surface. Each mapped area consists of 128×128 pixels with an area of $\approx 1280 \times 1280 \ \mu m^2$ (depending on the scan size which varied slightly between two sets of measurements). As a consequence of the much deeper proton penetration depth compared to the SEM electrons, PIXE analysis provides quantitative values of the layer thickness,

independent of any additional deposits of C and B residual impurities penetrating the gaps in the form of hydrogenated molecules [30]. Along the central scan line, five adjacent areas were measured with the final data array binned by eight pixels (i.e. an area of $80 \times 80 \ \mu m^2$) to reduce statistical error. The resulting profiles are also plotted in figure 11 with black markers whose width again corresponds to the respective binning range of $80 \ \mu m$.

The samples exposed in the reversed I_p and B_t experiment were additionally analysed at JSI using ^{3}He induced x-ray emission spectroscopy (^{3}HeIXE). In this case, Pt and W L_α transitions were excited by a 3 MeV ^{3}He ion beam focused to a surface spot of $15 \times 15 \ \mu m^2$ and respective line intensities evaluated in similar fashion to the EDX and PIXE measurements. Respective data are also plotted in figure 11 as green dots.

One sample pair (lower 1 mm gap) was also analysed with NRA using the reaction ^{3}He(^{12}C,p)^{14}N to quantify the area density of deposited C inside the gap by detecting the created protons. Due to the small cross-section of this reaction and the limited solid angle of the proton detector, corresponding data were binned over an area of 8×8 pixels (i.e. an area of $120 \times 120 \ \mu m^2$). These data points are also included in figure 11 with blue markers of respective width.

3.5. Erosion/deposition pattern in the gap

As mentioned in sections 3.3 and 3.4, the results of the EDX and ion micro beam measurements are plotted together with identical scaling in figure 11. The key point to note is the universal agreement of all data from the different analysis methods, demonstrating that the observed erosion and deposition patterns are not distorted by any systematic errors of the individual measurements.

In line with the visual evidence in the CLSM images (figure 10), the gap samples exposed in the reversed I_p and B_t experiment revealed complete erosion of the Pt marker layer to a depth of up to ≈ 1 mm inside the gap at the geometrically shadowed upper gap side face. The identical pattern is also seen in the corresponding W and C deposition profiles, with complete re-erosion of deposited species in the same depth range where the Pt marker layer has been fully eroded. SEM analysis in the zones of full Pt marker erosion further revealed roughening of the Mo substrate surface by crystal grain-dependent sputtering [31], indicating that erosion there continued well beyond complete removal of the Pt layer. These observations are perfectly in line with the expected erosion pattern due to gyrating ions entering the gap volume and hitting the geometrically shadowed upper gap side face as illustrated in figure 2(*a*). Moreover, the zone of marker erosion and W re-erosion switches to the opposite bottom gap side face in the experiment with default I_p and B_t direction, again perfectly consistent with the correspondingly opposite direction of ion gyration.

At the side faces opposite the erosion zone, localised deposition of both the eroded Pt and the re-eroded W and C is found. The deposition patterns in the 1 mm gap are shallower and wider than their counterparts in the 0.5 mm gaps, indicating
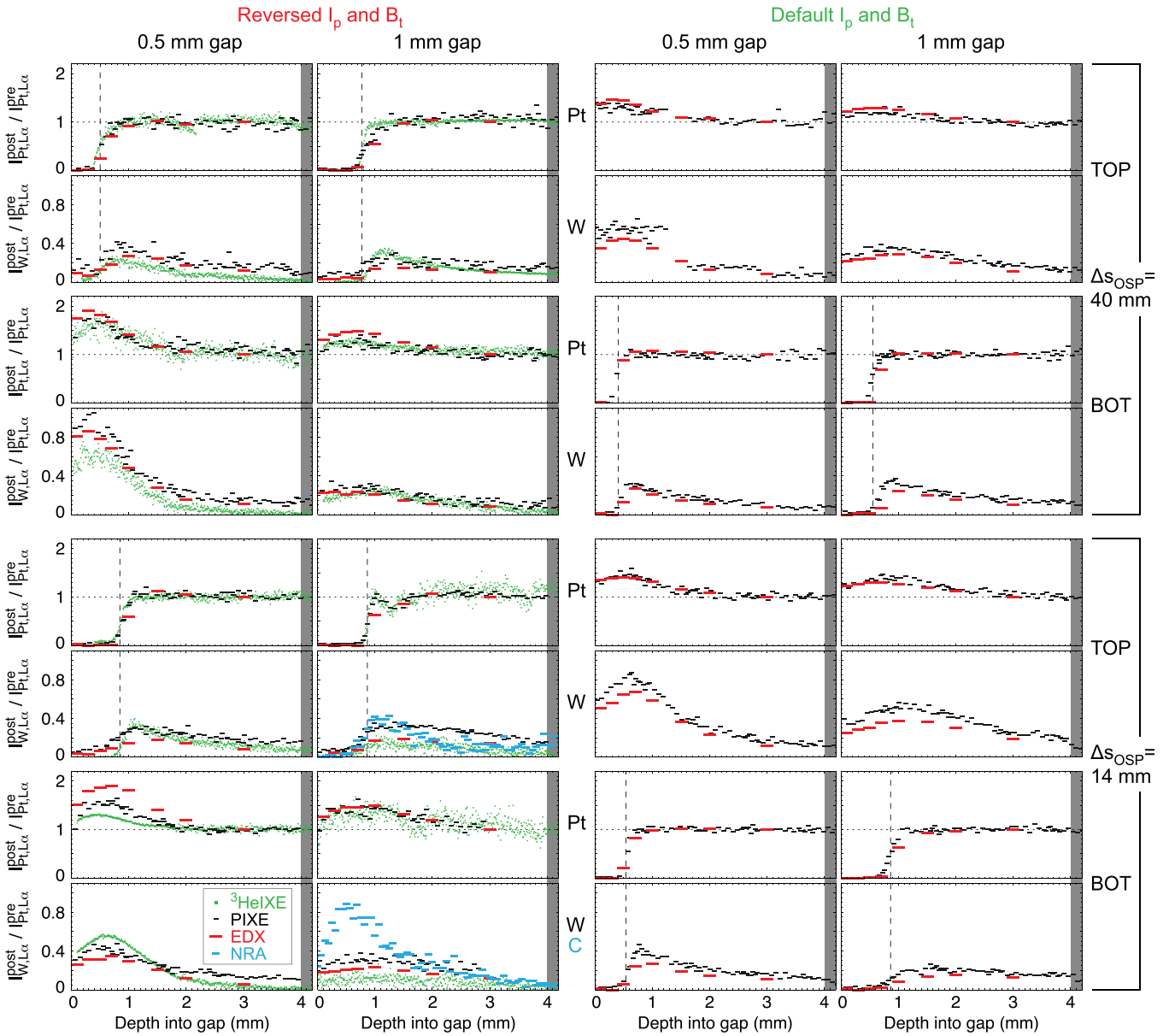
Figure 11. Profiles of post-exposure Pt marker layer thickness relative to pre-exposure thickness. The black lines represent the results of μ-beam PIXE analysis, the blue dots the results of μ-beam ^{3}HeIXE analysis. Red lines denote the results of EDX-SEM analysis. The depth of the marker erosion zones is indicated by dashed lines. All profiles were measured at the middle of the gap samples from the gap entrance down to the region covered by the steel spacer where the marker layers were protected from plasma exposure.

that with increasing gap width, eroded material can spread over a larger fraction of the opposite side face. The wider gap allows an increasing fraction of eroded material to escape the gap volume, which explains the lower maximum of the deposition profile.

4. Comparison with modelling

Given that the experimental evidence from the marker erosion inside the toroidal gap samples clearly indicates that the sputtering ions must have gyro radii in the mm range, comparison can be made with the expected ion energies during the ELM transients at the target plate.

The propagation of the pedestal plasma expelled by an ELM event into the SOL from the mid-plane to the divertor target has been described by a model assuming force free convective transport of a Maxwellian particle ensemble [8, 32], with similar results also obtained by kinetic numerical modelling [33]. In this model the characteristic ELM propagation time scale is given by $\tau_\| = L_\|^{\mathrm{ELM}}/c_s$ [32] with the sound speed $c_s = \sqrt{(T_e + T_i)/m_i}$ computed for temperature values at the pedestal top and $L_\|^{\mathrm{ELM}} = 2\pi q_{95}R$ where q_{95} is the safety factor at normalised radius $\rho_{\mathrm{pol}} = 0.95$ and R is the major plasma radius. For the discharges discussed here, $R = 1.62\,\mathrm{m}$ and $q_{95} \approx 5$ yielding $L_\|^{\mathrm{ELM}} \approx 50\,\mathrm{m}$. With the $\approx 1\,\mathrm{keV}$ pedestal temperature values (section 2.3), $c_s \approx 3.1 \times 10^5\ \mathrm{m\ s^{-1}}$

and thus $\tau_\parallel \approx 160\,\mu$s. This value is indeed compatible with the experimentally observed time delay between the upstream onset of an ELM transient and its arrival at the divertor plates, which defines $t = 0$ in the conditional average of the W_{MHD} signals shown in figure 4.

To verify that the ELM ions do not significantly thermalise during their transit from the upstream SOL to the target plates, this propagation time can be compared with the characteristic energy exchange time between ions and electrons $\tau_{\mathrm{ex}} = m_{\mathrm{i}}/2m_{\mathrm{e}}\,\tau_{\mathrm{e,i}}$ where $\tau_{\mathrm{e,i}} = 1.09 \times 10^{16}\,T_{\mathrm{e}}^{3/2}/n_{\mathrm{e}}\ln\Lambda$ (equation (14.6.1) in [34]). With $n_{\mathrm{e,ped}} \approx 3 \times 10^{19}\,\mathrm{m}^{-3}$ and $T_{\mathrm{e,ped}} = T_{\mathrm{i,ped}} \approx 1$ keV, $\tau_{\mathrm{ex}} \approx 20$ ms. It can therefore be concluded that the intra-ELM ion temperature at the target gap entrance is given approximately by T_{i} at the pedestal top for these discharge conditions.

Therefore, for the local magnetic field at the gap entrance of 2.6 T (table 2), the ELM-related ions with pedestal temperatures of $T_{\mathrm{i}} = 1$–1.2 keV can be assumed to enter the gap with gyro orbits of $r_{\mathrm{L}} = 1.75$–1.9 mm. In contrast, the Larmor radius of the inter-ELM ions, which are assumed to have $T_{\mathrm{i}} = T_{\mathrm{e}} < 25$ eV, is $r_{\mathrm{L}} < 0.28$ mm. It should be noted that residual low-Z impurity ions, which might provide a minor contribution to the marker erosion, have gyro radii in the same range for both intra-ELM and inter-ELM conditions. For example, carbon ions, here as proxy for the three species B, C and O, can be assumed in the intra-ELM phase to arrive from the pedestal as fully stripped C^{6+} ions [13] with $r_{\mathrm{L}} = 0.7$–0.8 mm in the intra-ELM range of T_{i}. For inter-ELM conditions, previous W-sputtering measurements indicated a lower average charge state of C^{3+}–C^{4+} [35]. For C^{3+} at $T_{\mathrm{i}} = 25$ eV, the gyro radius is $r_{\mathrm{L}} = 0.23$ mm, again similar to that of D^+.

For the interpretation of the observed erosion pattern, it is important to note that the trajectories of the hot ELM-related ions are collisionless on the length scale of the gap structure. This can be verified by comparing the ion gyro frequency $f_{\mathrm{ci}} = ZeB/(2\pi m_{\mathrm{i}}) \approx 20$ MHz to the ion–ion collision frequency $f_{\mathrm{ii}} = 1/\tau_{\mathrm{ii}}$ with $\tau_{\mathrm{ii}} = 6.60 \times 10^{17}\sqrt{m_{\mathrm{i}}/m_{\mathrm{p}}}\,T_{\mathrm{i}}^{3/2}/n_{\mathrm{e}}\ln\Lambda_{\mathrm{i}}$ (equation (14.6.2) in [34]), which gives, for $T_{\mathrm{i}} = 1$ keV, a collision frequency of 1 kHz.

The depth of the marker erosion zone, in both experiments, increases with the width of the toroidal gap. If the gyro radius of the incident ions were much smaller than the gap width, the extent of the eroded zone at the magnetically shadowed top side face in the reversed I_{p}, B_{t} configuration would be rather a function of the gyro radius alone, independent of the gap width. In contrast, for gyro orbits with a radius comparable to, or much larger than the gap width, the gap penetration depth of the ion trajectories is not only determined by their gyro radius but also limited by the scraping-off of ion orbits by the opposite gap edge and top surface (see figure 7 in [6]), with the cutoff ion fraction mainly determined by the gap width. Based on this observation, one can conclude that the gyro orbits of the ions, which caused the observed marker erosion, could not have been much smaller than the largest observed penetration depth. This qualitatively confirms that the ions causing the erosion must indeed have energies corresponding to the pedestal temperature and are therefore linked to the ELMs.

Furthermore, the depth of the erosion zone decreases with distance of the gap sample from the strike point, suggesting correspondingly lower ELM ion energies further out in the SOL.

In contrast, for inter-ELM conditions the gyro-radii of the ions are small enough that erosion by these ions would rather match the field line wetting pattern inside the gap, i.e. the corresponding erosion would occur at the lower gap side face up to a depth of $d = w \times \sin(B_z/|B|) \approx 0.03\,w$ with w being the gap width and local field values from table 2. Although Pt and W are not sputtered by deuterium ions at such low energies, the expected inter-ELM erosion at the bottom gap edge shows up in the carbon data. In contrast to Pt and W, the C deposition profile at the bottom side face in the reversed I_{p} and B_{t} scenario is indeed almost decreasing to zero towards the gap entrance.

Although the amount of Pt eroded during the entire exposure intervals cannot be determined (because in both experiments the marker layer in the erosion zone was completely removed), the known initial marker thickness allows at least a lower limit for the incident Larmor ion flux which caused the erosion to be determined. As discussed in section 3.1, the Pt marker on the samples in the reversed I_{p}, B_{t} experiment had an area density of $n_{\mathrm{a}}^{\mathrm{Pt}} = 126.5 \times 10^{15}$ at cm^{-2}. For incident deuterium ions during an ELM with $T_{\mathrm{i}} = 1$ keV and assuming intra-ELM $T_{\mathrm{e}} \approx 250$ eV [12], the sputter yield of Pt [36], averaged over the ion temperature distribution function, is $Y_{\mathrm{D}\to\mathrm{Pt}} \approx 0.024$. The additional contribution of the typically $<1\%$ fraction [37] of low-Z residual impurity ions is neglected here, because it is significantly smaller (e.g. $0.01 \times Y_{\mathrm{C}^{6+}\to\mathrm{Pt}} \approx 0.004$) and also more localised near the gap entrance because of the $\approx 50\%$ smaller r_{L}. Hence, the lower limit of ELM-related D^+ ion fluence for complete erosion of the Pt layer is $n_{\mathrm{a}}^{\mathrm{Pt}}/Y_{\mathrm{D}\to\mathrm{Pt}} = 5.3 \times 10^{22}\,\mathrm{m}^{-2}$.

With a total gap exposure time of $\Delta t = 20.2$ s, an ELM frequency of $f_{\mathrm{ELM}} = 135$ Hz (see table 1) and the hot ion fluence per ELM, Φ_{ELM}, derived in section 2.4 for the two sample positions, the total fluence of the ELM-related hot ions at the gap positions can be estimated to $\Delta t \times f_{\mathrm{ELM}} \times \Phi_{\mathrm{ELM}} = 19.4 \times 10^{22}\,\mathrm{m}^{-2}$ at the lower gap and $5.2 \times 10^{22}\,\mathrm{m}^{-2}$ at the upper gap.
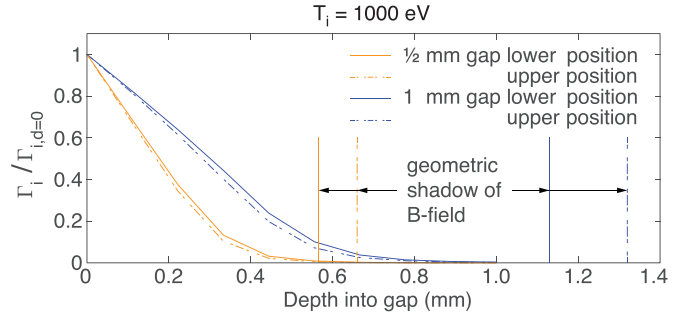
In the default I_{p}, B_{t} scenario, the Pt marker was thicker with $n_{\mathrm{a}}^{\mathrm{Pt}} = 339.8 \times 10^{15}$ at cm^{-2} and a resulting minimum D ion fluence of $14.1 \times 10^{22}\,\mathrm{m}^{-2}$ required to explain the complete removal of the marker layer in the erosion zone. The total ELM-related hot ion fluence at the respective gap entrance using the data in table 1 and section 2.4 can be estimated as for the first experiment, yielding values of $16.6 \times 10^{22}\,\mathrm{m}^{-2}$ at the lower gap and $5.9 \times 10^{22}\,\mathrm{m}^{-2}$ at the upper gap. Considering the uncertainties in the derived quantities due to the assumed sputtering yields and the extrapolation of pedestal temperatures to intra-ELM target plate quantities, the estimated ELM-related hot ion fluence values in both scenarios are fully compatible with the minimum deuterium flux values derived from the fully eroded Pt layer in the erosion zone.

A more detailed interpretation beyond these basic considerations requires numerical simulation of the local ion orbits
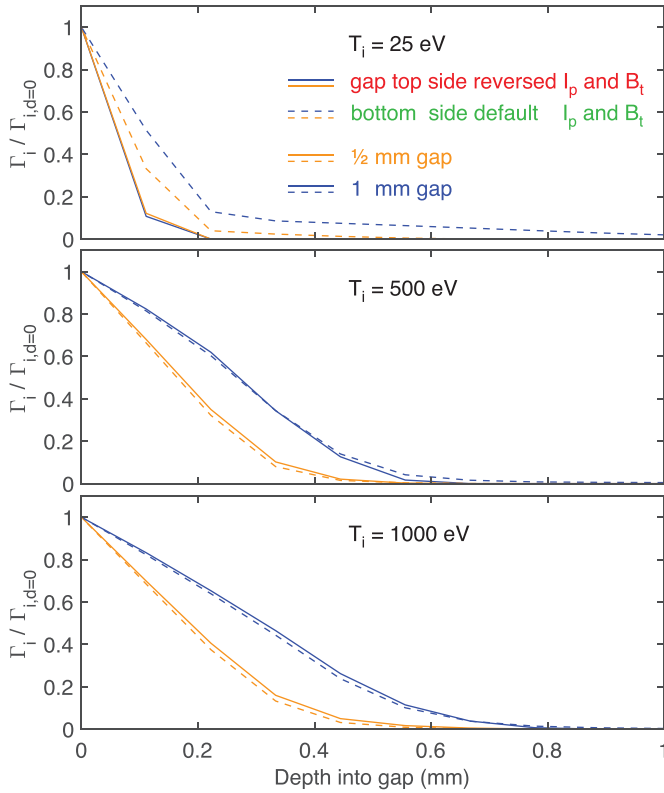
Figure 12. Ion orbit simulations of ion flux at the gap side face relative to the incident flux at the gap entrance for ion temperatures of $T_i = 25$ eV, $T_i = 0.5$ keV and $T_i = 1$ keV for the magnetic field geometry at the lower gap sample position at $s = 1.023$ m. The profiles calculated for a gap width of $w = 0.5$ mm are plotted in orange, those for $w = 1$ mm in blue. Solid lines refer to the ion flux to the top side face of the gaps in reversed I_p and B_t configuration, dashed lines to the ion flux to the bottom side face of the gaps in the default configuration.

Figure 13. Ion orbit simulation of the ion flux to the bottom gap side face relative to the incident flux at the gap entrance for default I_p, B_t configuration and $T_i = 1$ keV. Solid lines refer to profiles computed for the magnetic field geometry at the lower ($s = 1.023$ m) gap position, while dashed lines refer to profiles computed for the upper ($s = 1.054$ m) gap position. The profiles calculated for a gap width of $w = 0.5$ mm are plotted in orange, those for $w = 1$ mm in blue. The vertical lines denote the depth of the shadow cast by the upper toroidal gap edge with respect to the magnetic field.

above and inside the gap volume. From that the ion flux distribution on the inside surfaces of the gap volume can be computed. Using the model and code implementation described in [6] this was performed for the local magnetic field geometry and plasma conditions of the experiments discussed here. The resulting flux distribution relative to the flux at the gap entrance is shown in figure 12 for three different temperatures of the incident ions. Inter-ELM plasma conditions are represented by $T_i = 25$ eV. For the ELM D^+ ions, the simulations were run for two assumed ion temperatures representing the measured pedestal temperature, $T_i = 1$ keV and half of that value. For $T_i = 25$ eV, the ion flux arriving at the upper gap side face in reversed I_p and B_t configuration is focused on the first 0.1 mm, consistent with $r_L < 0.28$ mm, but much narrower than the measured Pt marker erosion depth range. It should be noted that at $T_i = 25$ eV the combined effective Pt sputtering yield by the incident deuterium flux and a 1% residual impurity fraction of $Y_{D \to Pt} + 0.01 \times Y_{C^{3+} \to Pt} \approx 10^{-3}$ is in any case too low to cause complete erosion of the marker layer. The inter-ELM ion flux profile at the bottom gaps side face in the default I_p and B_t configuration is slightly broader near the gap entrance, but also extends much further into the gap down to the limit given by the shadowing of the magnetic field lines

by the edges of the gap entrance (see figure 13). This is expected since at this low T_i, r_L is smaller than w and the distribution of incident ions still follows the geometric shadow pattern of the magnetic field lines.

For the typical ion pedestal temperature $T_i = 1$ keV and $r_L \approx 1.8$ mm $> w$, the profile of the incident ion flux is determined mainly by the gap width and the scraping off of the ion orbits by the edges of the gap entrance. In this range, the profiles at the ion orbit flux wetted side faces are therefore identical for both configurations of I_p and B_t (figure 12). Both the increase of gap penetration depth with gap width and with T_i are consistent with the experimental Pt erosion patterns shown in figure 11. Since the field line geometry at both gap positions is very similar, the simulations predict, as expected, only minor differences in the ion deposition profiles (see figure 13). It can thus be concluded from the simulation results that the experimentally observed shallower gap penetration on the samples further away from the OSP can be attributed to a lower ELM ion temperature there.

The good agreement of experimental data and ion orbit simulations is convincing evidence that the marker erosion is indeed caused by the impact of hot ELM-related ions. Moreover, if the erosion pattern is assumed to be given simply by the geometry of the magnetic field entering the gap volume and sputtering ion species with $r_L \ll w$, erosion of the marker layer should have occurred in both experiments at the lower gap side face, with the geometric plasma wetted area extending from the gap entrance to a depth of $d = B_z/B_y w \approx 1.1w$ (lower gap) and $w \approx 1.3w$ (upper gap). As a result of the gyro orbit motion, the actual extent of the eroded zone inside the gaps is, however, noticeably smaller than these values. This is also found in the experiment with default I_p and B_t directions. Furthermore, in the geometric approximation the upstream poloidal gap edge casts a field line shadow on the lower gap side face with its depth increasing in toroidal direction (see figure 14), whereas the experimentally observed erosion zones (figure 10) extend across a constant depth range over almost the entire toroidal gap length. The mismatch between
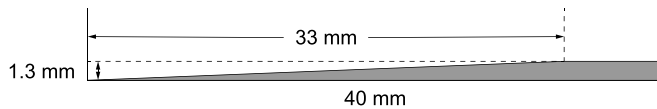
Figure 14. Geometric shadow cast by the upstream poloidal gap edge and upper toroidal gap edge with respect to the magnetic field on the bottom gap side face at the lower gap position. The horizontal coordinate represents the toroidal distance along the tile surface and the vertical coordinate denotes the gap depth.

the erosion patterns predicted by the geometric approximation and the experimental findings further supports the conclusion that the observed erosion is caused exclusively by the incident ELM-related hot ions and their corresponding ion orbit motion.

5. Discussion and conclusions

The experimental data presented here provide, for the first time, conclusive evidence for the significance of ion Larmor effects in the local distribution of the power flux at castellated divertor target components. The main observation in support of this conclusion is the reversal of the observed marker erosion on the side faces of the exposed gap samples with reversal of the magnetic field and plasma current directions (which reverses the ion orbit direction). Furthermore, the depth extent of the erosion patterns agrees with expected values and parametric dependencies from Larmor orbit size and gap width. In contrast, the erosion patterns are in contradiction to the pattern one would expect from the simple geometric approximation of guiding centre motion along magnetic field lines.

Together with the previous indirect observations based on IR thermography measurements of the temperature increase at the surface adjacent to the gap entrance [16–18], the results validate the predictive ion orbit simulations presented in [5–7]. The main caveat of the validation is the insufficient Pt marker layer thickness, which led to complete removal of the marker in the erosion zone so that the shape of the erosion profile could not be determined up to the gap edge for comparison with the code predictions. Even though it is assumed for the interpretation of the experiment that the ions striking the magnetically shadowed sides of the toroidal gaps are pure deuterium, the small contribution of impurity ions does not affect the conclusions drawn. The principle result of this work is that ions, whether they be fuel ions, or a mixture of fuel and impurity ions, strike the magnetically shadowed sides of the toroidal gaps, as predicted by ion orbit modelling and confirmed by PIC modelling.

In summary, the outcome of the study greatly increases confidence in the corresponding predictive simulations for the ITER tungsten divertor design [3], which highlights the importance of measures to reduce the energy density of ELM transients, either by dedicated mitigation techniques or by improved plasma operation scenarios. For the Type-I ELMy H-mode scenario, the experimental results support the FSM of ELM propagation [8], which predicts free convective transport

of the expelled pedestal plasma filaments from the upstream SOL to the divertor without significant thermalisation and thus with ion pedestal temperature retained when arriving at the divertor target.

Acknowledgments

ORCID iDs

K. Krieger ⬡ https://orcid.org/0000-0003-0427-8184
M. Balden ⬡ https://orcid.org/0000-0002-8755-9370
M. Barac ⬡ https://orcid.org/0000-0002-9504-9522
I. Bogdanović Radović ⬡ https://orcid.org/0000-0002-4100-736X
D. Brida ⬡ https://orcid.org/0000-0002-8647-7058
M. Faitsch ⬡ https://orcid.org/0000-0002-9809-7490
S. Markelj ⬡ https://orcid.org/0000-0002-6603-4006
A. Manhard ⬡ https://orcid.org/0000-0001-5242-9886
R.A. Pitts ⬡ https://orcid.org/0000-0001-9455-2698
V. Rohde ⬡ https://orcid.org/0000-0003-4895-7664

References

[1] Merola M., Escourbiac F., Raffray R., Chappuis P., Hirai T. and Martin A. 2014 Overview and status of ITER internal components *Fusion Eng. Des.* **89** 890–5
[2] Hirai T. *et al* 2014 ITER full tungsten divertor qualification program and progress *Phys. Scr.* **T159** 014006
[3] Pitts R.A. *et al* 2017 Physics conclusions in support of ITER W divertor monoblock shaping *Nucl. Mater. Energy* **12** 60–74
[4] Pitts R.A. *et al* 2019 Physics basis for the first ITER tungsten divertor *Nucl. Mater. Energy* **20** 100696
[5] Gunn J.P. *et al* 2017 Surface heat loads on the ITER divertor vertical targets *Nucl. Fusion* **57** 046025
[6] Gunn J.P. *et al* 2017 Ion orbit modelling of ELM heat loads on ITER divertor vertical targets *Nucl. Mater. Energy* **12** 75–83
[7] Gunn J.P., Hirai T., Corre Y., Escourbiac F., Grosjean A. and Pitts R.A. 2019 A study of planar toroidal-poloidal beveling of monoblocks on the ITER divertor outer vertical target *Nucl. Fusion* **59** 126043
[8] Fundamenski W. and Pitts R.A. (JET EFDA Contributors) 2006 A model of ELM filament energy evolution due to parallel losses *Plasma Phys. Control. Fusion* **48** 109–56
[9] Moulton D., Ghendrih P., Fundamenski W., Manfredi G. and Tskhakaya D. 2013 Quasineutral plasma expansion into infinite vacuum as a model for parallel ELM transport *Plasma Phys. Control. Fusion* **55** 085003

[10] Guillemaut C. *et al* 2015 Ion target impact energy during type I edge localized modes in JET ITER-like wall *Plasma Phys. Control. Fusion* **57** 085006

[11] Guillemaut C. *et al* 2018 Experimental validation of an analytical kinetic model for edge-localized modes in JET-ITER-like wall *Nucl. Fusion* **58** 066006

[12] Horacek J. *et al* 2023 ELM temperature in JET and COMPASS tokamak divertors *Nucl. Fusion* **63** 056007

[13] Abrams T. *et al* 2018 Experimental validation of a model for particle recycling and tungsten erosion during ELMs in the DIII-D divertor *Nucl. Mater. Energy* **17** 164–73

[14] Abrams T. *et al* 2019 Impact of ELM control techniques on tungsten sputtering in the DIII-D divertor and extrapolations to ITER *Phys. Plasmas* **26** 062504

[15] Komm M., Gunn J.P., Dejarnac R., Pánek R., Pitts R.A. and Podolník A. 2017 Particle-in-cell simulations of the plasma interaction with poloidal gaps in the ITER divertor outer vertical target *Nucl. Fusion* **57** 126047

[16] Hong S.H., Pitts R.A., Lee H.-H., Bang E., Kang C.-S., Kim K.-M. and Kim H.-T. 2017 Inter-ELM heat loads on tungsten leading edge in the KSTAR divertor *Nucl. Mater. Energy* **12** 1122–9

[17] Dejarnac R. *et al* 2018 Heat loads on poloidal and toroidal edges of castellated plasma-facing components in COMPASS *Nucl. Fusion* **58** 066003

[18] Dejarnac R., Gunn J.P., Vondracek P., Komm M., Panek R. and Pitts R.A. 2019 Physics of toroidal gap heat loading on castellated plasma-facing components *Nucl. Mater. Energy* **19** 19–27

[19] Herrmann A. *et al* 2015 A large divertor manipulator for ASDEX Upgrade *Fusion Eng. Des.* **98–99** 1496–9

[20] Chankin A.V. 1997 Classical drifts in the tokamak SOL and divertor: models and experiment *J. Nucl. Mater.* **241** 199–213

[21] Eich T., Sieglin B., Thornton A.J., Faitsch M., Kirk A., Herrmann A. and Suttrop W. 2017 ELM divertor peak energy fluence scaling to ITER with data from JET, MAST and ASDEX Upgrade *Nucl. Mater. Energy* **12** 84–90

[22] Wolfrum E. *et al* 2015 Overview of recent pedestal studies at ASDEX Upgrade *Nucl. Fusion* **55** 053017

[23] Viezzer E. *et al* 2013 High-accuracy characterization of the edge radial electric field at ASDEX Upgrade *Nucl. Fusion* **53** 053005

[24] Fischer R., Fuchs C.J., Kurzan B., Suttrop W. and Wolfrum E. 2010 Integrated data analysis of profile diagnostics at ASDEX Upgrade *Fusion Sci. Technol.* **58** 675–84

[25] Sieglin B., Eich T., Faitsch M., Herrmann A., Kirk A., Scarabosio A., Suttrop W. and Thornton A. 2017 Assessment of divertor heat load with and without external magnetic perturbation *Nucl. Fusion* **57** 066045

[26] Mc Carthy P.J. (ASDEX Upgrade Team) 2011 Identification of edge-localized moments of the current density profile in a tokamak equilibrium from external magnetic measurements *Plasma Phys. Control. Fusion* **54** 015010

[27] Weinlich M. and Carlson A. 1997 Flush mounted Langmuir probes in an oblique magnetic field *Phys. Plasmas* **4** 2151–60

[28] Brida D. *et al* 2017 Heat flux pattern in detached L-modes and ELM mitigated H-modes with rotating magnetic perturbations in ASDEX Upgrade *Nucl. Fusion* **57** 116006

[29] Rohde V., Balden M. and Neu R. (ASDEX Upgrade Team) 2021 Arc behaviour on different materials in ASDEX Upgrade *Nucl. Mater. Energy* **29** 101083

[30] Matveev D., Kirschner A., Litnovsky A., Komm M., Borodin D., Philipps V. and Van Oost G. 2010 Modelling of impurity deposition in gaps of castellated surfaces with the 3D-GAPS code *Plasma Phys. Control. Fusion* **52** 075007

[31] Schlueter K., Nordlund K., Hobler G., Balden M., Granberg F., Flinck O., da Silva T.F. and Neu R. 2020 Absence of a crystal direction regime in which sputtering corresponds to amorphous material *Phys. Rev. Lett.* **125** 225502

[32] Eich T., Kallenbach A., Fundamenski W., Herrmann A. and Naulin V. 2009 On the asymmetries of ELM divertor power deposition in JET and ASDEX Upgrade *J. Nucl. Mater.* **390–391** 760–3

[33] Tskhakaya D., Pitts R.A., Fundamenski W., Eich T. and Kuhn S. (JET EFDA Contributors) 2009 Kinetic simulations of the parallel transport in the JET scrape-off layer *J. Nucl. Mater.* **390–91** 335–8

[34] Wesson J. 1997 *Tokamaks* (*The Oxford Engineering Science Series*) 2nd edn (Oxford: Clarendon)

[35] Thoma A., Asmussen K., Dux R., Krieger K., Herrmann A., Napiontek B., Neu R., Steinbrink J., Weinlich M. and Wenzel U. (The ASDEX Upgrade Team) 1997 Spectroscopic measurements of tungsten erosion in the ASDEX Upgrade divertor *Plasma Phys. Control. Fusion* **39** 1487–99

[36] Eckstein W., Garćia-Rosales C., Roth J. and Ottenberger W. 1993 Sputtering data *Technical Report* IPP 9/82 (Max-Planck-Institut für Plasmaphysik Garching)

[37] Neu R. *et al* 2013 Overview on plasma operation with a full tungsten wall in ASDEX Upgrade *J. Nucl. Mater.* **438** S34–S41